Astronomy & Astrophysics manuscript no. irs48_coms_corrected
January 25, 2022

A major asymmetric ice trap in a planet-forming disk

III. First detection of dimethyl ether

Nashanty G.C. Brunken[1], Alice S. Booth[1], Margot Leemker[1], Pooneh Nazari[1], Nienke van der Marel[1], Ewine F. van Dishoeck[1,2]

[1] Leiden Observatory, Leiden University, 2300 RA Leiden, the Netherlands
e-mail: abooth@strw.leidenuniv.nl
[2] Max-Planck-Institut für Extraterrestrishe Physik, Gießenbachstrasse 1, 85748 Garching, Germany

Received; Accepted

ABSTRACT

The complex organic molecules (COMs) detected in star-forming regions are the precursors of the prebiotic molecules that can lead to the emergence of life. By studying COMs in more evolved protoplanetary disks we can gain a better understanding of how they are incorporated into planets. This paper presents ALMA band 7 observations of the dust and ice trap in the protoplanetary disk around Oph IRS 48. We report the first detection of dimethyl ether (CH_3OCH_3) in a planet-forming disk and a tentative detection of methyl formate (CH_3OCHO). We determined column densities for the detected molecules and upper limits on non-detected species using the CASSIS spectral analysis tool. The inferred column densities of CH_3OCH_3 and CH_3OCHO with respect to methanol (CH_3OH) are of order unity, indicating unusually high abundances of these species compared to other environments. Alternatively, the $^{12}CH_3OH$ emission is optically thick and beam diluted, implying a higher CH_3OH column density and a smaller emitting area than originally thought. The presence of these complex molecules can be explained by thermal ice sublimation, where the dust cavity edge is heated by irradiation and the full volatile ice content is observable in the gas phase. This work confirms the presence of oxygen-bearing molecules more complex than CH_3OH in protoplanetary disks for the first time. It also shows that it is indeed possible to trace the full interstellar journey of COMs across the different evolutionary stages of star, disk, and planet formation.

Key words. Astrochemistry, Stars: individual: Oph IRS 48, Planetary Systems: protoplanetary disks, Techniques: interferometric

1. Introduction

Complex organic molecules (COMs) are the precursors of prebiotic molecules, and thus understanding their formation and evolution will help us gain more insight into how life originated in our own Solar System (Caselli & Ceccarelli 2012). With new facilities such as the Atacama Large Millimeter/submillimeter Array (ALMA) and the Rosetta Orbiter Spectrometer for Ion and Neutral Analysis (ROSINA) on the Rosetta mission, we are now able to compare chemistry across a range of astronomical environments and get a better understanding of the chemical history of COMs throughout the entire star and planet-formation process, including comets (e.g. Drozdovskaya et al. 2019). It is crucial to study COMs in planet-forming disks in order to understand how the material in the disk is incorporated into planets and what degree of complexity is present at the epoch of planet formation (Öberg & Bergin 2021).

The formation of most of these COMs is thought to occur in cold molecular clouds (Boogert et al. 2015). During this time, atoms and simple molecules such as CO will stick to the dust grains forming an ice layer and undergo chemical reactions (e.g. Herbst & van Dishoeck 2009; Chuang et al. 2018; Ioppolo et al. 2021). The products are subsequently released back into the gas phase if there is an increase in temperature resulting in thermal desorption. Additionally, molecules will also return to the gas phase via other processes such as UV photodesorption, but this can lead to the fragmentation of the molecule when it enters the gas phase (Garrod et al. 2006; Cruz-Diaz et al. 2016). COMs are therefore especially abundant in the gas phase in young warm systems where they are easily detected because of thermal sublimation ($T_{\rm dust} > 100$ K) (e.g., Bergner et al. 2017; Jørgensen et al. 2018; van Gelder et al. 2020; Mercimek et al. 2021; Belloche et al. 2020). This is in contrast to older protoplanetary disks which are colder and thus the COMs remain frozen on dust grains in the bulk of the disk and are therefore more often undetectable in the gas phase with ALMA (van 't Hoff et al. 2020). However, COMs are expected to be abundant in protoplanetary disk ices and there is some evidence for this in the outbursting protostellar source V883 Ori which is rich in COMs (van 't Hoff et al. 2018; Lee et al. 2019).

The current situation is that, in protoplanetary disks of more than 1 Myr old, even the most abundant complex organic molecule (COM), methanol (CH_3OH), is difficult to detect. CH_3OH is a cornerstone in the chemistry leading to many larger complex organic molecules (Öberg et al. 2009). Walsh et al. (2016) presented the first detection of CH_3OH in the TW Hya protoplanetary disk. However, the fractional abundance relative to H_2 is very low (3×10^{-12} - 4×10^{-11}), indicating a chemical origin in the gas phase via inefficient and fragmenting non-thermal desorption of the ices rather than thermal sublimation (Walsh et al. 2017). Carney et al. (2019) also provided an upper limit on the abundance of CH_3OH in the Herbig Ae disk HD 163296 of $< 1.6 \times 10^{-12}$ relative to H_2. For comparison, CH_3OH abundances in hot protostellar cores are typically of order 10^{-6}, comparable to those in ices (Boogert et al. 2015).

More recently, Booth et al. (2021) detected CH_3OH for the first time in a warm Herbig transition disk. In comparison to the ringed CH_3OH emission in TW Hya the CH_3OH in the HD 100546 disk originates from the inner 50 au of the disk and its likely origin is thermal desorption. Because Herbig Ae/Be sources like this one are inherently warm, which prevents freeze-out of the precursor CO, in situ formation of the CH_3OH is unlikely. Instead the presence of CH_3OH in the disk can be explained via the inheritance of COM-rich ices from colder parent molecular clouds.

Also, another Herbig source was revealed to have a rich observable chemistry: the IRS 48 transition disk (van der Marel et al. 2014; van der Marel et al. 2021b; Booth et al. 2021). What makes this disk particularly interesting is the fact that it contains a highly asymmetric dust trap of large grains ($\gtrsim$ 0.1 mm) on the southern side of the star, making it the most asymmetric disk detected to date (van der Marel et al. 2013; van der Marel et al. 2021a). van der Marel et al. (2021b) report the detection of CH_3OH and formaldehyde (H_2CO) in this disk. The emissions have the same crescent shape as the dust continuum, showing for the first time the direct link between a dust trap and COMs. This coincidence was hinted at with low signal-to-noise H_2CO observations (van der Marel et al. 2014) but is now confirmed. The bulk of the ice reservoir of the IRS48 disk is constrained to the larger dust grains, and because of UV irradiation from the central star, the dust temperature increases enough to liberate the CH_3OH from the ices. Booth et al. (2021) additionally report the detection of SO_2 in the IRS 48 dust trap, the first detection of this molecule in a protoplanetary disk, along with detection of SO. The detection of these molecules supports the presence of oxygen-rich gas where the C/O < 1 because of sublimated ices.

In this paper, we report the analysis of ALMA data of IRS 48 including the first detection of dimethyl ether (CH_3OCH_3) in a protoplanetary disk and a tentative detection of methyl formate (CH_3OCHO). CH_3OCH_3 is the largest complex organic molecule that has been detected in a protoplanetary disk to date. We also report the first detection of nitric oxide (NO) in a protoplanetary disk, which will be analysed in a future paper. Our paper is structured as follows: In Section 2 we describe our observational methods and in Section 3 we show our data analysis and provide the values for the derived column densities. In Section 4 we discuss the chemistry of the detected species, compare abundances to other astronomical environments, and determine upper limits for other molecules covered in the data. Finally, in Section 5 we give a short summary and provide conclusions.

2. Observations

Our data were taken with ALMA. The Band 7 line data (~ 0.8mm) were taken on August 18, 2018 (2017.1. 00834.S, PI: Adriana Pohl), and the continuum data presented in Figure 1 were taken in June and August 2015 (2013.1.00100.S, PI: Nienke van der Marel). Ohashi et al. (2020) provide a full description of the line data calibration. In papers I and II, we cover the detections of CH_3OH, H_2CO, SO, and SO_2 (van der Marel et al. 2021b; Booth et al. 2021) and in this paper we present the detection of CH_3OCH_3 and NO, and investigate other tentative detections and upper limits.

Data reduction was done using the Common Astronomy Software Applications (CASA)[1] version 5.7.0. The spectral windows have channel widths of ~ 1.7 km s^{-1} and a beam size of 0.″55×0.″42 (PA = 80°). The spectral windows have central frequencies of 349.7, 351.5, 361.6, and 363.5 GHz, respectively, with SPW1 from 349.79 to 350.66 GHz, SPW2 from 350.60 to 352.47 GHz, SPW3 from 360.68 to 362.55 GHz, and SPW4 from 362.61 to 364.47 GHz. We imaged the data with the `tclean` function in CASA using a Briggs weighting with a robust value of 0.5. The image was recentred to the star position using the phase centre parameter in CASA and was set to ICRS 16:27:37.17 -24:30:35.55. We used a Keplerian mask over the region of emission at a distance of 136 pc (Gaia Collaboration et al. 2021), an inclination angle of 50 °, and a position angle of 100 ° (van der Marel et al. 2021a).

The cleaned images were subsequently stacked using GoFish version 1.3.6 (Teague 2019) in order to increase the signal-to-noise ratio. This method makes it possible to identify potential weak lines and also distinguish between lines that are blended (very close in frequency). We extract spectra over the whole azimuth of the disk although the lines are co-spatial with the dust trap. This is done because the observations are not well spatially resolved. The spectra for the four spectral windows are shown in the Appendix Figures B1-B4.

3. Analysis

3.1. Spectral analysis

The stacked, continuum-subtracted spectra were analysed using the CASSIS[2] spectral analysis tool version 5.1.1 (Vastel et al. 2015) in a similar way to that used by Nazari et al. (e.g., 2021). The flux densities were first converted to brightness temperature units and local thermodynamic equilibrium (LTE) conditions were assumed in order to derive the column densities and excitation temperatures. We made use of the Cologne Database for Molecular Spectroscopy (CDMS) (Müller et al. 2001, 2005) and the Jet Propulsion Laboratory (JPL) database (Pickett et al. 1998) for molecular information. In Table A.1 we list the transitions of the detected species. The integrated intensity maps of selected lines are presented in Figure 1. The search for other potential features in the spectra was carried out by making a selection of commonly detected COMs in other environments and only taking into account lines with $E_{up} \leq 400$ K and $A_{ul} \geq 1\times_{10}{}^{-6}$ s^{-1}. For this selection of molecules, we modelled the spectra in CASSIS by assuming an excitation temperature of 100 K motivated by the rotational temperature derived by van der Marel et al. (2021b) for the CH_3OH. We also calculated the best-fit column density at both 70 K and 250 K to have an estimate of the column density error for the detected species, which is typically a factor of two. The absolute calibration error is much smaller, of order 10%, and this will cancel out in abundance ratios. We used a FWHM of ~ 7 km s^{-1} based on the line width of a strong CH_3OH line and a source size of 1.4 × 10 $^{-11}$ sr based on the 5 σ emission continuum of the disk (Figure 1), the same as in van der Marel et al. (2021b); Booth et al. (2021). Using these variables we derived column densities and upper limits. We note that the inferred column density, N, scales inversely with the assumed emitting area, Ω_{source} (Goldsmith & Langer 1999), that is,

$$N \propto \frac{1}{\Omega_{source}}. \quad (1)$$

[1] https://casa.nrao.edu/index.shtml

[2] http://cassis.irap.omp.eu

In the case where the source does not fill the beam, the column density will be underestimated by a dilution factor:

$$\text{Dilutionfactor}^{-1} = \frac{\Omega^2_{\text{source}}}{\Omega^2_{\text{beam}} + \Omega^2_{\text{source}}}, \quad (2)$$

where Ω_{beam} is the beam size (e.g. van Gelder et al. 2020).

3.2. Revising the CH_3OH column density

We first modelled the CH_3OH lines in our spectra based on the parameters derived in van der Marel et al. (2021b). Using CASSIS we find models consistent with the data using a column density for CH_3OH of $5 \times_{10}{}^{14}$ cm^{-2} and an excitation temperature of 100 K which is in agreement with the rotational diagram analysis of van der Marel et al. (2021b). These results are shown in Figure 2. However, in this work, additional CH_3OH transitions are detected and these are highlighted in Table A1. Figure 1 shows the integrated intensity maps of a CH_3OH line with an upper energy level of 333 K. We also detect two weaker lines in the stacked spectra that are better fit at a higher column density of 2×10^{15} cm^{-2} and still at a temperature of 100 K (see Figure 2 for a comparison of the two models). These two lines are the $9_{-5,4}$ - $9_{-4,6}$ and $3_{1,2}$ - $4_{2,2}$ at 351.236 GHz (E_{up} = 241 K, $\log_{10}(E_{\text{A}})$ = −4.44 s^{-1}) and 361.236 GHz (E_{up} = 339 K, $\log_{10}(E_{\text{A}})$ = −3.58 s^{-1}) respectively. Both lines were visible in our stacked spectra at the 2.5-3σ level but neither one was detected in the channel maps above the 3 σ level. These weak lines are reproduced at a different column density, which likely indicates that the emission traced by the stronger lines is optically thick. van der Marel et al. (2021b) calculate the optical depth of these lines and show they are optically thin for the assumed emitting area. The difference between this and our result can be resolved if the lines are optically thick and beam diluted, because the column density is inversely proportional to the assumed emitting area. We also derived a 3σ upper limit for the column density of $^{13}CH_3OH$ of $< 5.5 \times 10^{14}$ cm^{-2}. This gives a strict upper limit on the CH_3OH column density of $\approx 3.3 \times 10^{16}$ cm^{-2} assuming a $^{12}C/^{13}C$ ratio of 60. This upper-limit is consistent with the column density found via the weakest CH_3OH lines. We use $N(CH_3OH) = 2 \times 10^{15}$ cm^{-2} as a reference for comparisons.

3.3. Detection of dimethyl ether and methyl formate

We detect two sets of blended lines for CH_3OCH_3. See Table A.1 for the transition information, Figure 1 for an intensity-integrated map of one of the sets of blended lines, and Figure C.1 for the channel maps of both. We derive a column density of $1.5 \times_{10}{}^{15}$ cm^{-2} at an assumed excitation temperature of 100 K; see Figure 2 for the CASSIS model fits. The excitation temperature of CH_3OCH_3 may be lower than that of CH_3OH (e.g. Jørgensen et al. 2018) but given that only a few transitions are detected, we calculate the column densities over a range of excitation temperatures from 80 to 250 K (listed in Table 1). We also found a tentative detection of CH_3OCHO after modelling several features in our spectra. One such emission feature with a S/N above 3σ noise level can be seen at 363.48 and 363.49 GHz (Figure 2). We show a clear > 5 σ detection of a line in the channel maps at this frequency range (Figure C.2) and the integrated intensity map is shown in Figure 1. While the modelled spectrum of CH_3OCHO does not provide an exact fit for the emission feature, it is the closest fit found after considering other possible candidates. Furthermore, the model spectrum for CH_3OCHO fits several other smaller features in the spectra (see Figures B.1,B.2,B.3,B.4). From these models we derive a best-fit column density of 1.3×10^{15} cm^{-2} at an excitation temperature of 100 K.

3.4. Other line detections and upper limits

We detect a total of five transition lines for nitric oxide (Table A.1). This is the first detection of NO in a protoplanetary disk. We were alerted to the possible presence of NO in our disk when we encountered a difficulty in fitting the bright CH_3OH line at 350.68 GHz (Figure 2). NO has two transitions at this frequency, but a single line was not enough to confirm a definitive detection of the molecule because this line is also blended with CH_3OH. We are able to prove the presence of NO in the disk after successfully fitting an additional double feature at 351.04 and 351.05 GHz (Figure 2). From the CASSIS spectral analysis models, we derive a best-fit total column density for NO of $3 \times_{10}{}^{15}$ cm^{-2} at an excitation temperature of 40 K. The NO lines have a low excitation temperature (36 K) compared to many of the COM lines detected and the lower temperature best fits the multiple lines. The NO lines will be more quantitatively analysed in a future paper.

We also detect an additional SO_2 line at 363.16 GHz (Figure B.1) that was not reported in Booth et al. (2021). The column densities from our spectral analysis are in agreement with their value.

Finally, we also derive upper limits for species that remain undetected in the IRS 48 disk but that have been observed in younger sources and other older disks such as formic acid (t-HCOOH), acetaldehyde (CH_3CHO), and methyl cyanide (CH_3CN) (e.g., Bergner et al. 2017; Favre et al. 2018; van Gelder et al. 2020; Ilee et al. 2021). These upper limits are listed in Table 1.

4. Discussion

We find a wealth of molecular complexity in the IRS 48 disk, including the first detections of multiple molecules in disks. In this section, we discuss the chemical origin of the COMs, compare relative abundances to other environments, and consider the prospects for further complexity in the disk.

4.1. Chemical origin of the COMs

The observed CH_3OH emission in the IRS 48 disk first presented by van der Marel et al. (2021b) is azimuthally co-spatial with the dust trap and peaking at slightly smaller radius. van der Marel et al. (2021b) proposed that the presence of CH_3OH in the disk is due to thermal ice sublimation and that the ice reservoir is constrained to the larger millimetre-sized grains. Vertical mixing in the vortex may also help in lifting icy dust grains to the warm surface. CH_3OH forms on CO ice via a sequence of H-addition reactions with key intermediates HCO and H_2CO (Fuchs et al. 2009; Chuang et al. 2017). Because the grain surface chemistry of CH_3OH is related to both CH_3OCH_3 and CH_3OCHO, particularly in the presence of UV radiation, we expect that both of these COMs also originate from the sublimating ices (Öberg et al. 2009), Garrod & Herbst (2006) and Garrod et al. (2008) provide a theoretical model in which complex organic molecules, including CH_3OCH_3 and CH_3OCHO, can form via cold grain-surface reactions (≤ 50 K) involving radicals:

$$CH_3O + HCO \longrightarrow CH_3OCHO, \quad (3)$$

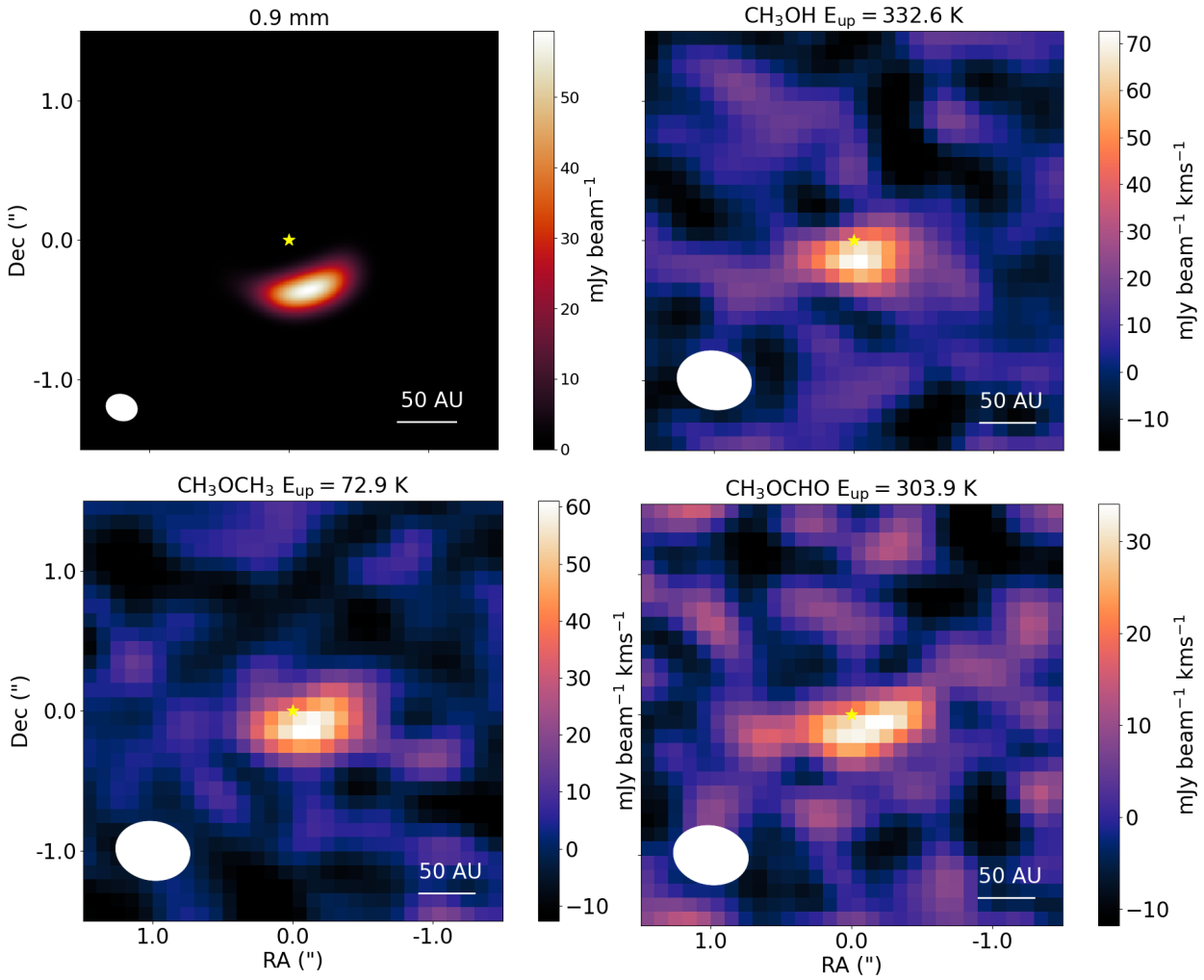

Fig. 1. Integrated intensity maps of the 0.9 mm continuum emission and a subset of the detected molecular lines listed in Table A.1. Top right is the CH_3OH $16_{1,15}$ - $16_{0,16}$, bottom left is the CH_3OCH_3 $11_{3,8}$−$10_{2,9}$, and bottom right is the CH_3OCHO $32_{2,30}$−$32_{2,29}$ and $32_{3,30}$−$32_{3,29}$ blend. The beam is shown in the bottom left corner and a scale bar is shown in the bottom right corner.

$$CH_3O + CH_3 \longrightarrow CH_3OCH_3. \quad (4)$$

This model shows a common formation route from the methoxy precursor CH_3O. These pathways have also been shown to be present in laboratory experiments (Chuang et al. 2016). These COMs could nevertheless be further enhanced due to UV irradiation of the ices from the central star resulting in photodissociation of CH_3OH (Öberg et al. 2009; Walsh et al. 2014),

$$CH_3OH + h\nu \longrightarrow CH_3 + OH \text{ or } CH_3O + H, \quad (5)$$

where the dissociation products can then recombine via reactions (1) and (2).

4.2. Comparisons to other environments

CH_3OCH_3 is the largest complex organic molecule detected in a protoplanetary disk. It has been detected in several other, younger sources (e.g. Taquet et al. 2015; Soma et al. 2018; Bergner et al. 2018). We compare our results as summarised in Table 1 (100 K column) and Figure 3 with the observed abundances in other astronomical environments including the class 0 protostellar binary IRAS 16293 A and B (Jørgensen et al. 2018; Manigand et al. 2020), the outbursting source V883 Ori (Lee et al. 2019), and the comet 67P (Drozdovskaya et al. 2019). The high observed CH_3OCH_3/CH_3OH ratio in the IRS 48 disk, of order unity, is different from that in the other sources by a factor of 5-10 (Figure 3). The abundance derived for CH_3OCHO also shows a similar trend to CH_3OCH_3 in that CH_3OCHO seems to be more abundant compared to the other sources. The high derived column-density ratios of CH_3OCH_3/CH_3OH and CH_3OCHO/CH_3OH in IRS 48 (Figure 3) compared to other environments may be due to optically thick CH_3OH emission that is beam diluted resulting in over-estimated abundance ratios. To increase the optical depth in CH_3OH to the amount that would make the ratio consistent with other sources, an area of order 10^{-12} sr would be needed. If the emission is constrained to the inner edge of the dust cavity, this would require a crescent shape for the emitting area with a length of ≈1.″0, corresponding to a width of ≈0.″1 in COM emission, which could be resolved in future higher resolution data. Detections of CH_3OH isotopologues are needed to determine whether optical depth is indeed the cause of the difference or chemical processing in the disk relative to ices in dark clouds and young stars could be responsible for the enhanced chemical complexity in the UV-irradiated ice trap.

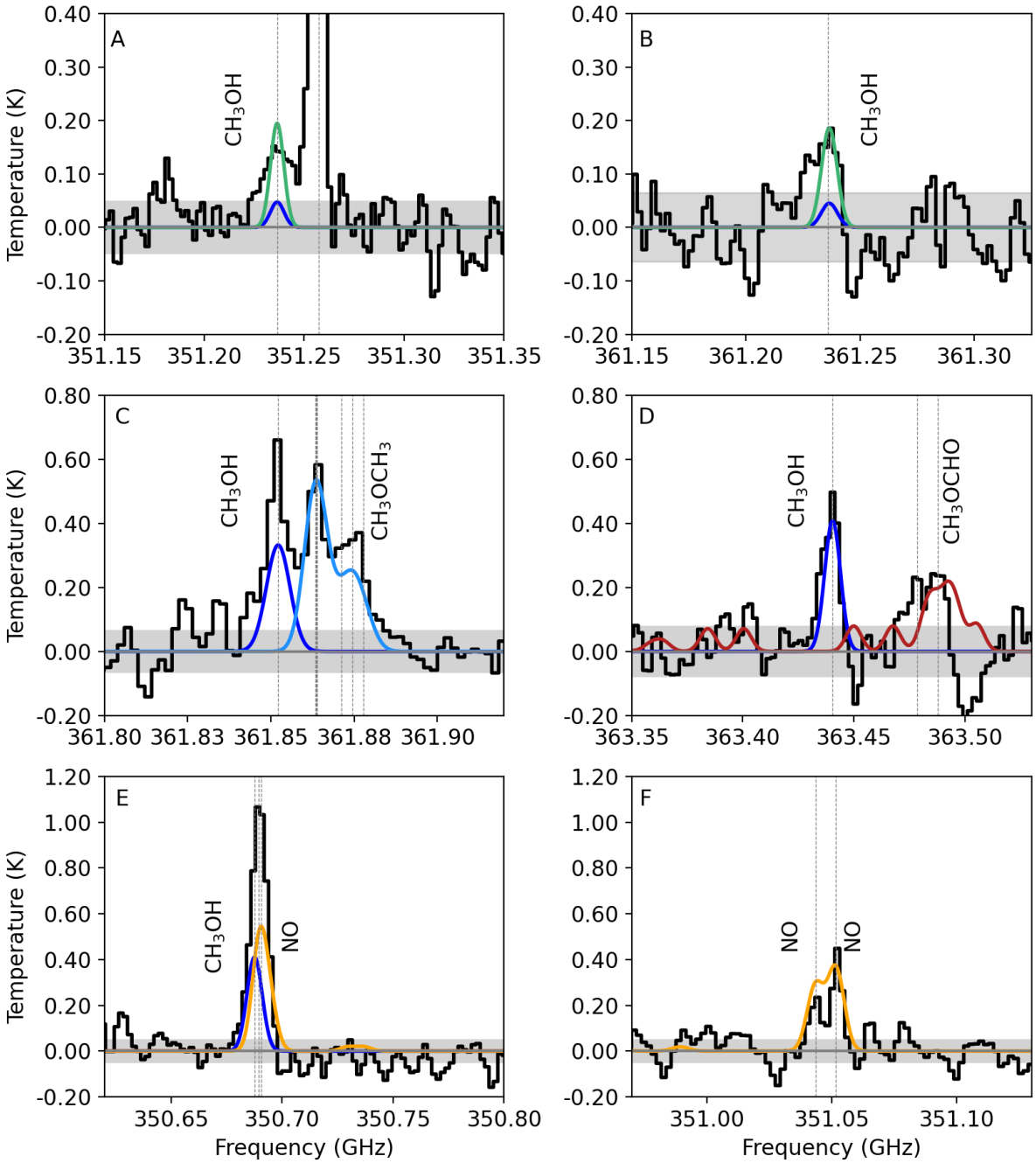

Fig. 2. Stacked continuum-subtracted spectra (black lines) and CASSIS models (coloured lines) for the molecules detected in this work. Dashed lines mark the frequencies of the transitions as listed in Table 1 and the grey bar marks the $\pm 1\sigma$ error calculated from the line-free channels in each spectral window. Panels A and B show the two weak CH_3OH lines $9_{-5,4}$ - $9_{-4,6}$ and $3_{1,2}$ - $4_{2,2}$ with the 100 K CASSIS models at 5×10^{14} cm^{-1} (blue) and 2×10^{15} cm^{-1} (green). Panels C and D show the best-fit models for the CH_3OCH_3 $20_{1,20}$–$19_{0,19}$ and $11_{3,8}$-$10_{2,9}$ transitions and the CH_3OCHO $32_{3,30}$-$31_{3,29}$ and $32_{3,30}$-$31_{2,29}$ transitions. In panel D the negative dip in the spectrum at ≈363.5 GHz may be an atmospheric absorption feature (https://almascience.eso.org/about-alma/atmosphere-model). Panels E and F show the best-fit models for NO covering the 4_1-4_3 and 4_1-4_4 transitions. Panels C, D, and E also show the CH_3OH model for the strong lines.

The CH_3OCH_3/CH_3OCHO ratio in our disk is approximately 0.9 and this is consistent with what is observed in other sources across a full range of environments from star and disk formation to comets (Coletta et al. 2020). This adds further evidence that these two species are likely chemically related to one another and points towards ice formation of both molecules and therefore the inheritance of ices in the IRS 48 disk.

4.3. Upper limits

We also derived upper limits for the column densities of COMs that were previously detected in other sources. These molecules are listed in Table 1; see also Figure 3. Although CH_3CHO, t-HCOOH, and CH_3CN have been detected in several sources, we note that they remain absent in our disk despite having formation routes via grain-surface chemistry (Walsh et al. 2014).

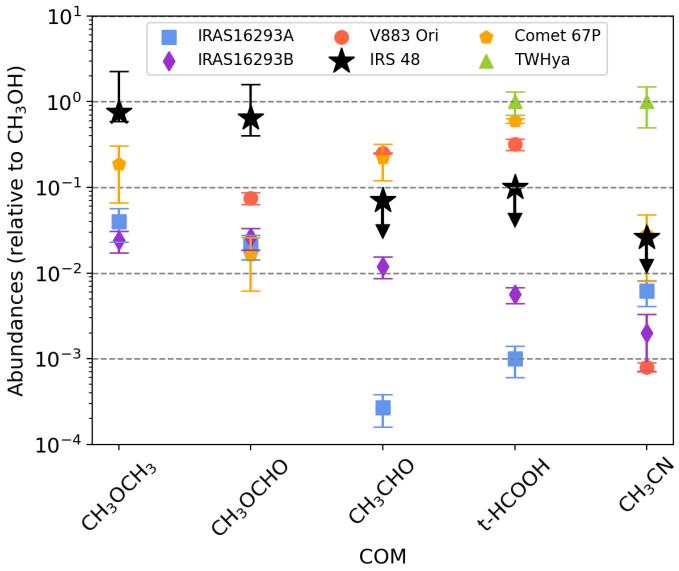

Fig. 3. Abundances of commonly detected COMs relative to CH_3OH. Solid squares show the detections in IRS 48 and arrows show the non-detected species for which upper limits on the column density are derived. The error bars on the IRS 48 points come from calculating the column densities over a range of excitation temperatures. For the other sources, see references in Section 4.

In particular, HCOOH can form via the HCO or HOCO radicals and CH_3CHO via the CH_3 and HCO radicals. The non-detection of formic acid is potentially interesting, as in disk chemical models it is predicted to have a similar fractional abundance to CH_3OH in the gas phase (Walsh et al. 2014). From the upper limit, we constrain this ratio to <10 %. However, Walsh et al. (2014) predict that the CH_3OH ice column density is approximately ten times higher than HCOOH. This could explain the non-detection of HCOOH in our data if the sublimating ice reservoir is the primary origin of both molecules. TW Hya also has a detection of formic acid (Favre et al. 2018) and in this disk the t−HCOOH/CH_3OH abundance ratio is approximately unity. This is at least an order of magnitude higher than the 1%-10% seen in young stars and comets (e.g. Drozdovskaya et al. 2019). In comparison to IRS 48, where the observable chemistry appears to be dominated by ice sublimation, TW Hya is a cold disk where small amounts of COMs in the gas phase are due to non-thermal desorption and/or gas-phase chemistry.

Similarly, with the detection of CH_3OCH_3 we might also expect to have detected CH_3CHO. The abundance of CH_3CHO with respect to CH_3OH is found to be about ten times lower thanthat of CH_3OCH_3. This difference is consistent with the results of van Gelder et al. (2020) who find lower abundances of CH_3CHO compared to CH_3OCH_3 in young protostellar envelopes.

Another molecule that is particularly interesting to look at is CH_3CN as it has been detected in multiple protoplanetary disks (Loomis et al. 2018; Bergner et al. 2018; Ilee et al. 2021). The formation of CH_3CN seems to be dominated by gas-phase chemistry but grain surface processes cannot be neglected (Loomis et al. 2018). In particular, gas-phase CH_3CN is enhanced in environments with high C/O ratio. In TW Hya, the only disk with detections of both CH_3OH and CH_3CN the CH_3CN/CH_3OH column density ratio is approximately unity. Unlike what we expect for IRS 48, in TW Hya the observable CH_3CN and CH_3OH likely do not have the same chemical origin. The CH_3CN is primarily formed via gas-phase routes whereas the CH_3OH most likely originates from the ices (Loomis et al. 2018; Walsh et al. 2016, 2017). In IRS 48 we have an upper limit of ≈10%. This is in better agreement with the 1%-10% seen in comets and young stars (see Figure 3 and e.g. Bergner et al. 2017).

We also obtained upper limits on the deuterated form of methanol CH_2DOH. The upper limit on this column density at an excitation temperature of 100 K is $6.0 \times {}_{10}{}^{14}$ cm^{-2}. This then gives an upper limit on the D/H of 10% and this is consistent with the ratios seen in protostellar cores, young low-mass stars, and comet 67P (≈1%-10%, e.g. van Gelder et al. 2020; Drozdovskaya et al. 2021).

4.4. Prospects for further complexity in the IRS 48 ice trap

Confirmation of the CH_3OCHO detection is needed because our models do not fit the emission feature very well and we only have one significant feature to fit given the frequency coverage of the observations. There are several other COMs that remain undetected in our disk and which should be the focus of future work. The molecules listed in Table 1 are examples of species that should be searched for in future studies due to the fact that most have been detected in multiple protostellar sources. The detection of CH_3OCH_3 and CH_3OCHO alongside CH_3OH implies a rich ice chemistry in the IRS 48 dust trap. Other COMs which have related formation routes via the radials HCO, CH_3O and CH_2OH including ethylene-glycol, acetaldehyde, ethanol, and glycolaldehyde, should be subject of follow-up observations.

5. Conclusions

We analyzed ALMA data of the IRS 48 transition disk, revealing a wealth of molecular complexity.

- We report the first detections of dimethy ether (CH_3OCH_3), nitric oxide (NO), and a tentative detection of methyl formate (CH_3OCHO) in a protoplanetary disk.
- We report an additional detection of a SO_2 transition in the disk with an upper energy level of ≈250 K.
- The emissions of the detected species show a direct link with the asymmetric dust trap in the southern region of the disk, further suggesting that molecular complexity in this disk is due to ice sublimation.
- The abundance ratios of CH_3OCH_3 and CH_3OCHO compared with CH_3OH are high relative to other environments. This either means that these molecules are enhanced relative to CH_3OH in this disk or that the CH_3OH column density we derive is underestimated. The latter situation could be due to the lines being optically thick but beam diluted. A higher CH_3OH column density would mean a COM-emitting area smaller than the assumed area, the 5σ extent of the millimetre dust trap. With further high-angular-resolution observations, we will be able to determine whether or not the emitting area is truly just the thin inner edge of the dust trap.
- The detection of CH_3OCH_3 and CH_3OCHO in such a warm disk and the agreement in the CH_3OCH_3/CH_3OCHO column density ratio with other environments strengthens the case for an origin inherited from the cold cloud phase, but the abundances with respect to CH_3OH may be enhanced because of UV irradiation.

Hopefully future observations of the IRS 48 icy dust trap will allow for the detection of other COMs and more robust constraints on the column density and excitation conditions. This work is an important puzzle piece in tracing the full interstellar

Table 1. Derived column densities and upper limits

Species	Name	Column density (cm^{-2}) T_{ex} = 100 K	Column density (cm^{-2}) T_{ex} = 70 - 250 K
CH_3OH	Methanol	2×10^{15}	$1.0 - 2.5 \times 10^{15}$
CH_3OCH_3	Dimethyl ether	1.5×10^{15}	$1.5 - 3.5 \times 10^{15}$
CH_3OCHO	Methyl formate	1.3×10^{15}	$1.0 - 2.5 \times 10^{15}$
$^{13}CH_3OH$	Methanol	$< 5.5 \times 10^{14}$	-
CH_2DOH	Methanol	$< 6.0 \times 10^{14}$	-
t−HCOOH	Formic Acid	$< 2.0 \times 10^{14}$	-
CH_3CN	Methyl cyanide	$< 1.3 \times 10^{13}$	-
CH_3CHO	Acetaldehyde	$< 1.4 \times 10^{14}$	-
CH_3COOH	Acetic acid	$< 3.4 \times 10^{15}$	-
$CH_2(OH)CHO$	Glycoaldehyde	$< 1.8 \times 10^{14}$	-
CH_3SH	Methyl mercaptan	$< 4.0 \times 10^{14}$	-
D_2CO	Formaldehyde	$< 4.5 \times 10^{13}$	-
HC_3N	Cyanoacetylene	$< 2.2 \times 10^{13}$	-
HNC	Hydrogen cyanide	$< 1.5 \times 10^{12}$	-
HNCO	Isocyanic acid	$< 4.5 \times 10^{13}$	-
NH_2CH_2COOH	Glycine, conf. I	$<4.5 \times 10^{15}$	-
NH_2CH_2COOH	Glycine, conf. II	$< 5.5 \times 10^{14}$	-

Molecular information was obtained using the JPL and CDMS database (Müller et al. 2001, 2005; Pickett et al. 1998). The spectra were modelled using the CASSIS spectral analysis tool. For the detected lines, a range of T_{ex} from 70 K to 250 K was modelled. The 3 σ upper limits were derived assuming a T_{ex} of 100 K.

journey of COMs across the different evolutionary stages of star, disk, and planet formation.

Acknowledgements. Astrochemistry in Leiden is supported by the Netherlands Research School for Astronomy (NOVA). ALMA is a partnership of ESO (representing its member states), NSF (USA) and NINS (Japan), together with NRC (Canada) and NSC and ASIAA (Taiwan) and KASI (Republic of Korea), in cooperation with the Republic of Chile. The Joint ALMA Observatory is operated by ESO, AUI/ NRAO and NAOJ. This paper makes use of the following ALMA data: 2013.1.00100.S, 2017.1.00834.S.

References

Belloche, A., Maury, A. J., Maret, S., et al. 2020, A&A, 635, A198
Bergner, J. B., Guzmán, V. G., Öberg, K. I., Loomis, R. A., & Pegues, J. 2018, The Astrophysical Journal, 857, 69
Bergner, J. B., Öberg, K. I., Garrod, R. T., & Graninger, D. M. 2017, The Astrophysical Journal, 841, 120
Boogert, A. C. A., Gerakines, P. A., & Whittet, D. C. B. 2015, ARA&A, 53, 541
Booth, A. S., van der Marel, N., Leemker, M., van Dishoeck, E. F., & Ohashi, S. 2021, A&A, 651, L6
Booth, A. S., Walsh, C., van Scheltinga, J. T., et al. 2021, Nature Astronomy, 1
Carney, M., Hogerheijde, M., Guzmán, V., et al. 2019, Astronomy & Astrophysics, 623, A124
Caselli, P. & Ceccarelli, C. 2012, A&A Rev., 20, 56
Chuang, K. J., Fedoseev, G., Ioppolo, S., van Dishoeck, E. F., & Linnartz, H. 2016, MNRAS, 455, 1702
Chuang, K. J., Fedoseev, G., Qasim, D., et al. 2017, MNRAS, 467, 2552
Chuang, K. J., Fedoseev, G., Qasim, D., et al. 2018, A&A, 617, A87
Coletta, A., Fontani, F., Rivilla, V., et al. 2020, Astronomy & Astrophysics, 641, A54
Cruz-Diaz, G. A., Martín-Doménech, R., Muñoz Caro, G. M., & Chen, Y. J. 2016, A&A, 592, A68
Drozdovskaya, M. N., Schroeder I, I. R. H. G., Rubin, M., et al. 2021, MNRAS, 500, 4901
Drozdovskaya, M. N., van Dishoeck, E. F., Rubin, M., Jørgensen, J. K., & Altwegg, K. 2019, Monthly Notices of the Royal Astronomical Society, 490, 50
Drozdovskaya, M. N., van Dishoeck, E. F., Rubin, M., Jørgensen, J. K., & Altwegg, K. 2019, MNRAS, 490, 50
Favre, C., Fedele, D., Semenov, D., et al. 2018, ApJ, 862, L2
Fuchs, G. W., Cuppen, H. M., Ioppolo, S., et al. 2009, A&A, 505, 629
Gaia Collaboration, Brown, A. G. A., Vallenari, A., et al. 2021, A&A, 649, A1
Garrod, R. & Herbst, E. 2006, Astronomy & Astrophysics, 457, 927
Garrod, R., Park, I. H., Caselli, P., & Herbst, E. 2006, Faraday Discussions, 133, 51
Garrod, R. T., Weaver, S. L. W., & Herbst, E. 2008, The Astrophysical Journal, 682, 283
Goldsmith, P. F. & Langer, W. D. 1999, ApJ, 517, 209
Herbst, E. & van Dishoeck, E. F. 2009, Annual Review of Astronomy and Astrophysics, 47, 427
Ilee, J. D., Walsh, C., Booth, A. S., et al. 2021, ApJS, 257, 9
Ioppolo, S., Fedoseev, G., Chuang, K. J., et al. 2021, Nature Astronomy, 5, 197
Jørgensen, J., Müller, H., Calcutt, H., et al. 2018, Astronomy & Astrophysics, 620, A170
Lee, J.-E., Lee, S., Baek, G., et al. 2019, Nature Astronomy, 3, 314
Loomis, R. A., Cleeves, L. I., Öberg, K. I., et al. 2018, The Astrophysical Journal, 859, 131
Manigand, S., Jørgensen, J., Calcutt, H., et al. 2020, Astronomy & Astrophysics, 635, A48
Mercimek, S., Codella, C., Podio, L., et al. 2021, arXiv e-prints, arXiv:2111.07573
Müller, H. S., Schlöder, F., Stutzki, J., & Winnewisser, G. 2005, Journal of Molecular Structure, 742, 215
Müller, H. S., Thorwirth, S., Roth, D., & Winnewisser, G. 2001, Astronomy & Astrophysics, 370, L49
Nazari, P., van Gelder, M., van Dishoeck, E., et al. 2021, Astronomy & Astrophysics, 650, A150
Öberg, K. I. & Bergin, E. A. 2021, Phys. Rep., 893, 1
Öberg, K. I., Garrod, R. T., Van Dishoeck, E. F., & Linnartz, H. 2009, Astronomy & Astrophysics, 504, 891
Ohashi, S., Kataoka, A., Van der Marel, N., et al. 2020, The Astrophysical Journal, 900, 81
Pickett, H., Poynter, R., Cohen, E., et al. 1998, Journal of Quantitative Spectroscopy and Radiative Transfer, 60, 883
Soma, T., Sakai, N., Watanabe, Y., & Yamamoto, S. 2018, The Astrophysical Journal, 854, 116
Taquet, V., López-Sepulcre, A., Ceccarelli, C., et al. 2015, The Astrophysical Journal, 804, 81
Teague, R. 2019, Journal of Open Source Software, 4, 1632
van der Marel, N., Birnstiel, T., Garufi, A., et al. 2021a, AJ, 161, 33
van der Marel, N., Booth, A. S., Leemker, M., van Dishoeck, E. F., & Ohashi, S. 2021b, A&A, 651, L5
van der Marel, N., van Dishoeck, E., Bruderer, S., & van Kempen, T. 2014, Astronomy & Astrophysics, 563, A113
van der Marel, N., Van Dishoeck, E. F., Bruderer, S., et al. 2013, Science, 340, 1199
van Gelder, M. L., Tabone, B., Tychoniec, Ł., et al. 2020, A&A, 639, A87
van 't Hoff, M. L. R., Harsono, D., Tobin, J. J., et al. 2020, arXiv e-prints, arXiv:2008.08106

van 't Hoff, M. L. R., Tobin, J. J., Trapman, L., et al. 2018, The Astrophysical Journal, 864, L23
Vastel, C., Bottinelli, S., Caux, E., Glorian, J., & Boiziot, M. 2015, in SF2A-2015: Proceedings of the Annual meeting of the French Society of Astronomy and Astrophysics, 313–316
Walsh, C., Herbst, E., Nomura, H., Millar, T. J., & Weaver, S. W. 2014, Faraday discussions, 168, 389
Walsh, C., Loomis, R. A., Öberg, K. I., et al. 2016, The Astrophysical Journal Letters, 823, L10
Walsh, C., Vissapragada, S., & McGee, H. 2017, Proceedings of the International Astronomical Union, 13, 395

Appendix A: Table of molecular lines detected

Appendix B: Spectra

Table A.1. Properties of the molecular lines analysed in this work.

Molecule	Transition	Frequency (GHz)	$\log_{10}(A_{ij})$ (s^{-1})	E_u (K)	g_u	Reference
CH_3OH	$14_{1,13}$ - $14_{0,14}$	349.106997	-3.356	260.2	116	van der Marel et al. (2021b)
CH_3OH[1]	$4_{0,4}$ - $3_{1,3}$	350.687662	-4.0619	36.3	36	van der Marel et al. (2021b)
CH_3OH	$1_{1,1}$ - $0_{0,0}$	350.905100	-3.4795	16.8	12	van der Marel et al. (2021b)
CH_3OH[2]	$9_{-5,4}$ - $9_{-4,6}$,	351.236479	-4.43803	240.5	76.0	This work
CH_3OH	$11_{0,11}$ - $10_{1,9}$	360.848946	-3.9183	166.0	92	van der Marel et al. (2021b)
CH_3OH[2]	$3_{1,2}$ - $4_{2,2}$	361.236506	-3.57681	339.2	28.0	This work
CH_3OH	$8_{1,7,1}$ - $7_{2,6,1}$	361.852195	-4.1125	104.6	68	van der Marel et al. (2021b)
CH_3OH	$16_{1,15}$ - $16_{0,16}$	363.440442	-3.3179	332.6	132	This work
CH_3OH	$7_{2,6}$ - $6_{1,5}$	363.739868	-3.7677	87.3	60	van der Marel et al. (2021b)
CH_3OCH_3[3]	$20_{1,20}$ - $19_{0,19}$	361.863445	-3.4051	184.5	164	This work
CH_3OCH_3[3]	$20_{1,20}$ - $19_{0,19}$ AE + EA	361.863446	-3.4051	184.5	246	This work
CH_3OCH_3[3]	$20_{1,20}$ - $19_{0,19}$ EE	361.863547	-3.4051	184.5	656	This work
CH_3OCH_3[3]	$20_{1,20}$ - $19_{0,19}$ AA	361.863648	-3.405	184.5	410	This work
CH_3OCH_3[3]	$20_{1,20}$ - $19_{0,19}$ AE	361.863693	-3.2054	184.5	123	This work
CH_3OCH_3[3]	$20_{1,20}$ - $19_{0,19}$ EE	361.863782	-3.2055	184.5	328	This work
CH_3OCH_3[3]	$20_{1,20}$ - $19_{0,19}$ AA	361.863871	-3.2055	184.5	205	This work
CH_3OCH_3	$11_{3,8}$ - $10_{2,9}$ AE	361.871157	-3.6652	72.9	69	This work
CH_3OCHO[4]	$32_{3,30}$ - $31_{3,29}$ E	363.482855	-3.16595	303.9	65	This work
CH_3OCHO[4]	$32_{3,30}$ - $31_{2,29}$ E	363.482881	-3.14442	303.9	130	This work
CH_3OCHO[4]	$32_{2,30}$ - $31_{2,29}$ E	363.485165	-3.16594	303.9	65	This work
CH_3OCHO[4]	$32_{2,30}$ - $31_{2,29}$ E	363.485187	-3.14442	303.9	130	This work
CH_3OCHO[4]	$32_{2,30}$ - $31_{3,29}$ A	363.487618	-3.89252	303.9	65	This work
CH_3OCHO[4]	$32_{2,30}$ - $31_{3,29}$ A	363.487661	-4.02862	303.9	130	This work
CH_3OCHO[4]	$32_{3,30}$ - $31_{2,29}$ A	363.488265	-3.89249	303.9	65	This work
CH_3OCHO[4]	$32_{3,30}$ - $31_{2,29}$ A	363.488271	-4.02872	303.9	130	This work
CH_3OCHO[4]	$32_{3,30}$ - $31_{3,29}$ E	363.490703	-3.16593	303.9	65	This work
CH_3OCHO[4]	$32_{3,30}$ - $31_{3,29}$ E	363.490764	-3.14442	303.9	130	This work
NO[1]	4_{1} - 4_{3}	350.689494	-5.2662	36.2	10.0	This work
NO[1]	4_{1} - 4_{3}	350.690766	-5.3032	36.2	8.0	This work
NO[5]	4_{1} - 4_{3}	351.043524	-5.2649	36.2	10.0	This work
NO[5]	4_{1} - 4_{4}	351.051705	-5.3019	36.2	8.0	This work
NO[5]	4_{1} - 4_{3}	351.051705	-5.316	36.2	6.0	This work
SO_2	$21_{4,18}$ - $21_{3,19}$	363.159262	-3.397	252.1	43.0	This work

The line frequencies, Einstein A coefficients, upper energy levels (E_{up}), and degeneracies (g_u) are taken from the Cologne Database for Molecular Spectroscopy (CDMS) (Müller et al. 2001, 2005; Pickett et al. 1998). [1]Blended methanol and nitric oxide lines. [2] Weak methanol lines fitted at a different column density.[3]Blended dimethyl ether lines. [4]Blended methyl formate lines. [5]Blended nitric oxide lines.

Appendix C: Channel maps

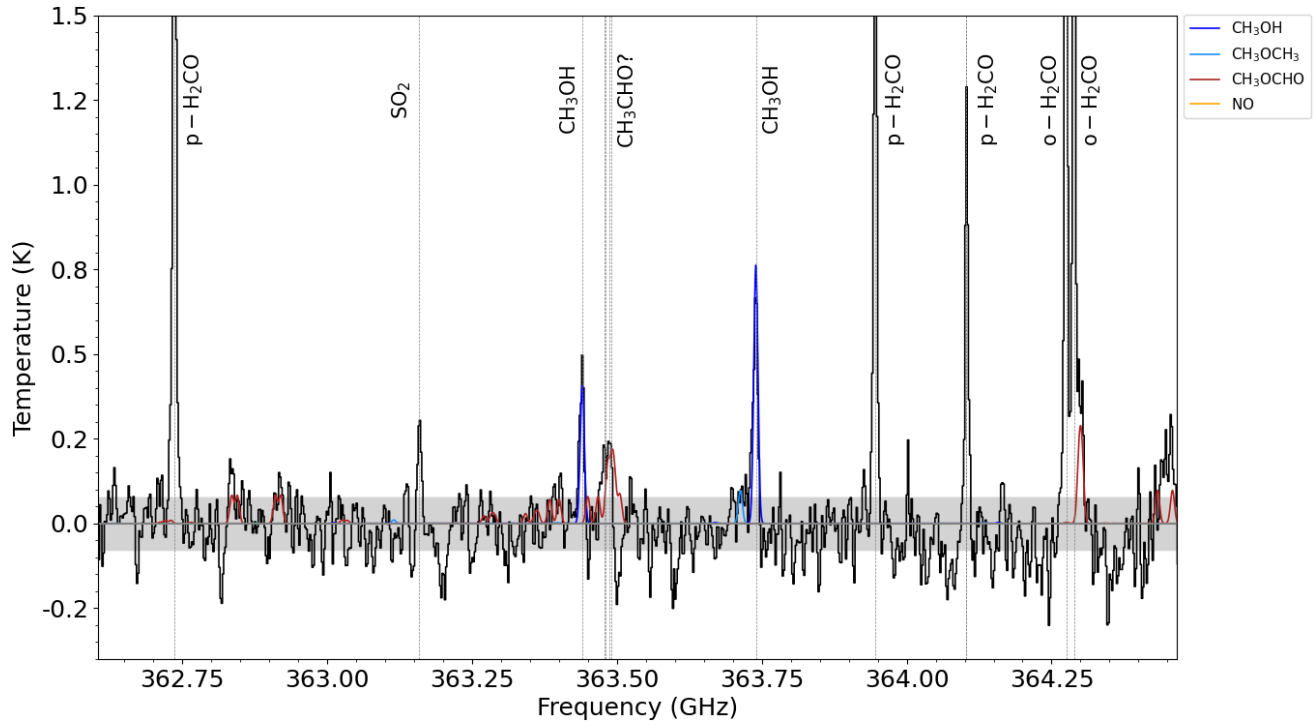

Fig. B.1. Stacked spectra with CASSIS model fits with T_{ex} = 100 K for all species aside from NO which is modelled at 40 K. The grey region shows the +/- 1σ error. The vertical dashed lines denote the rest frequency of the lines. The CH_3OH model is with a column density of $5{\times}10^{14}$ cm^{-2}. In Figure 2 we show how a higher column density better fits weaker CH_3OH lines covered in the observations.

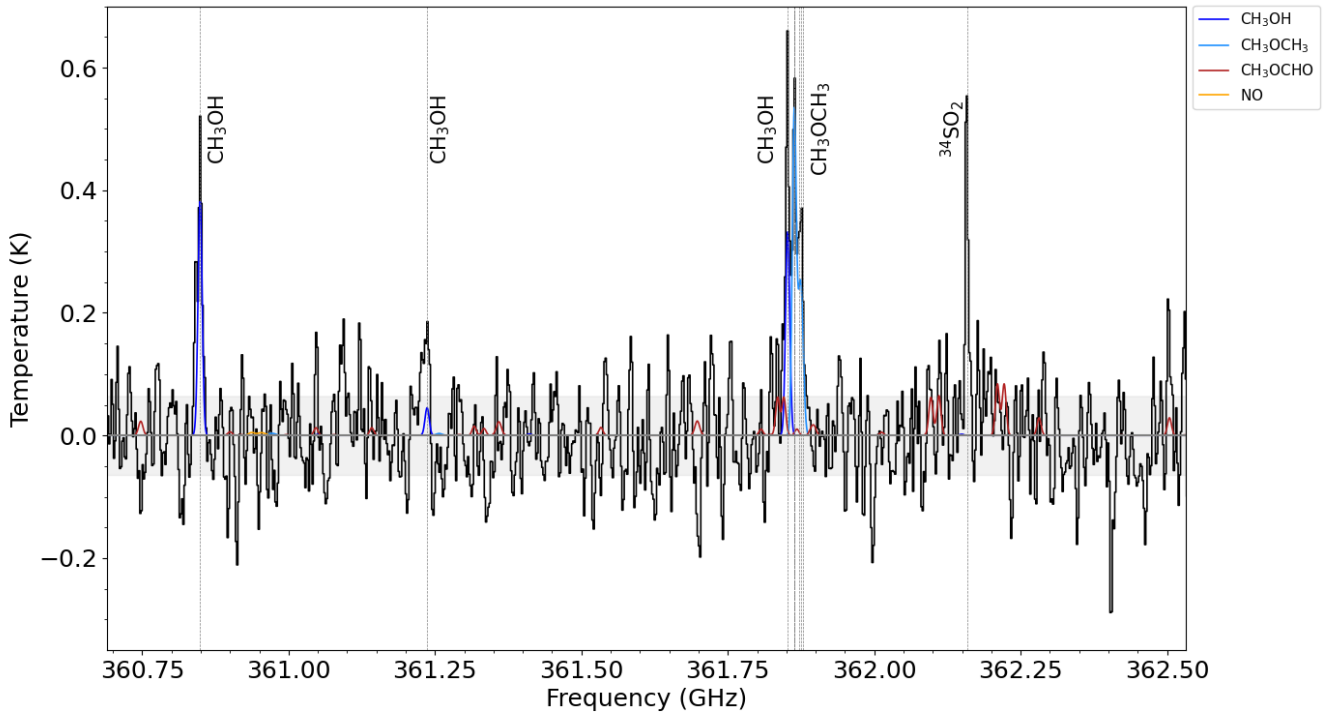

Fig. B.2. Same as Figure B.1

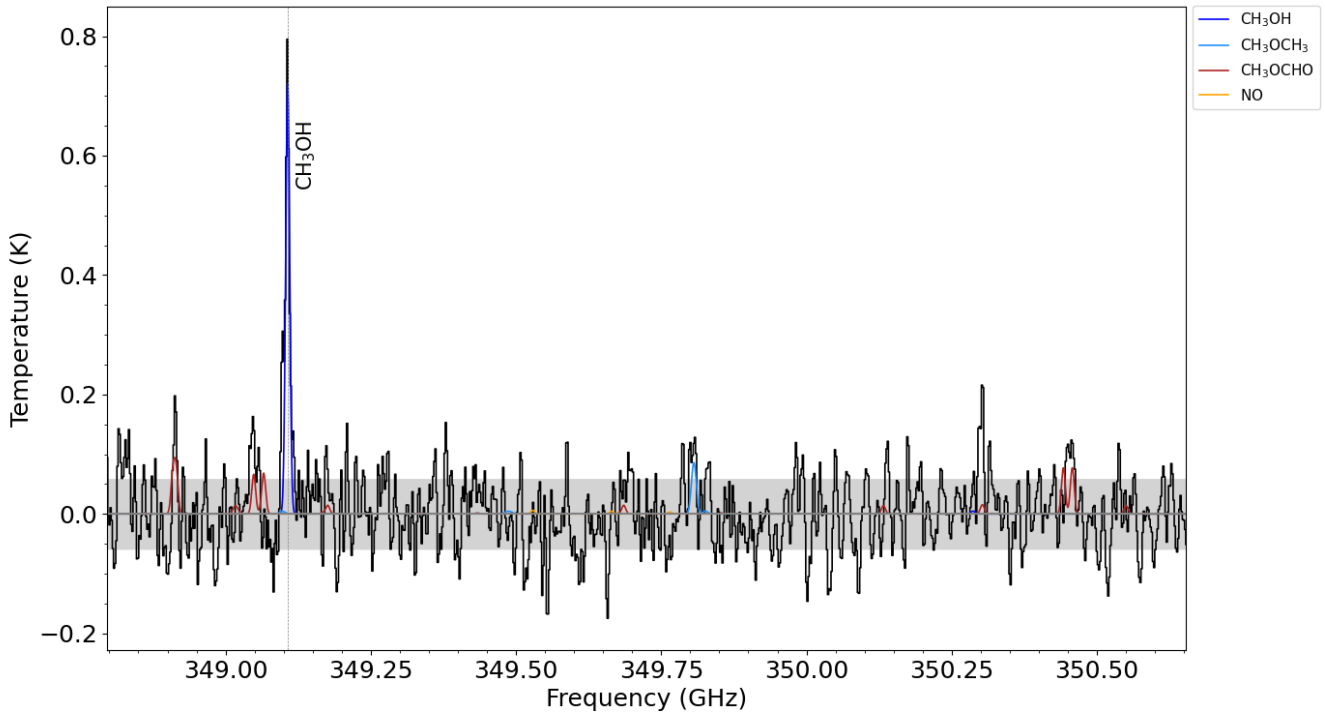

Fig. B.3. Same as Figure B.1

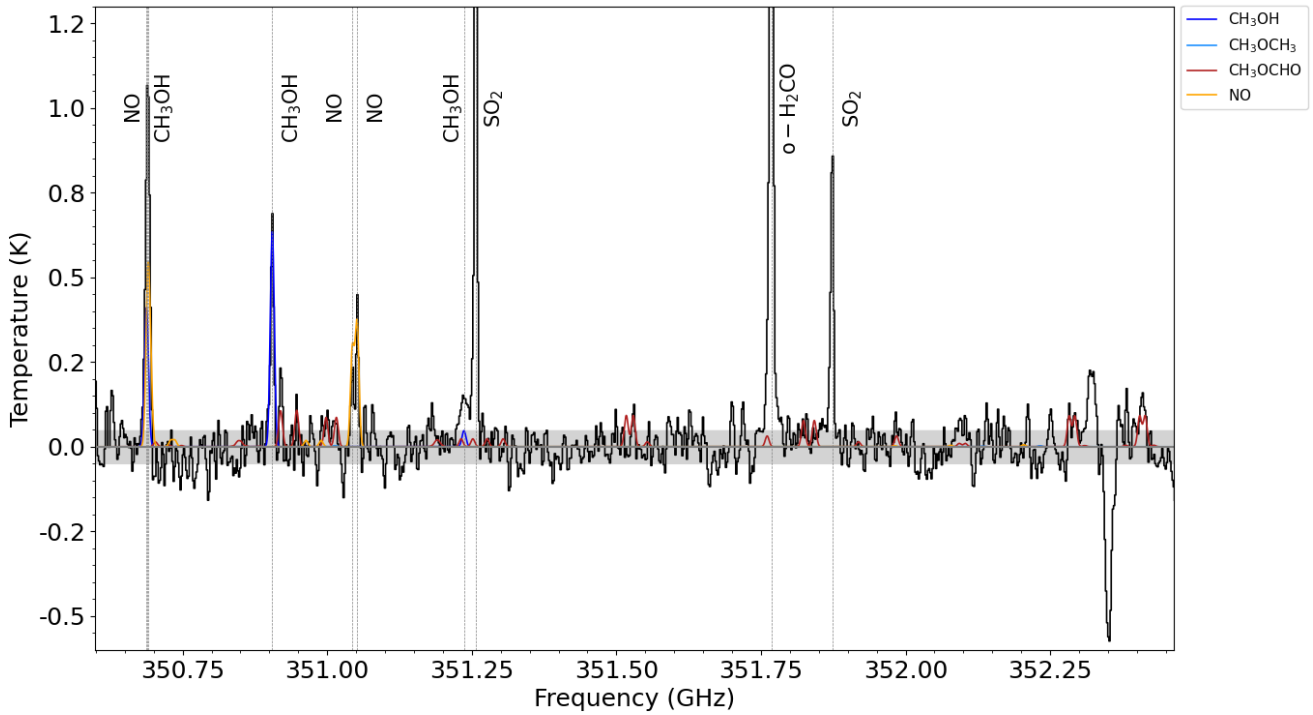

Fig. B.4. Same as Figure B.1

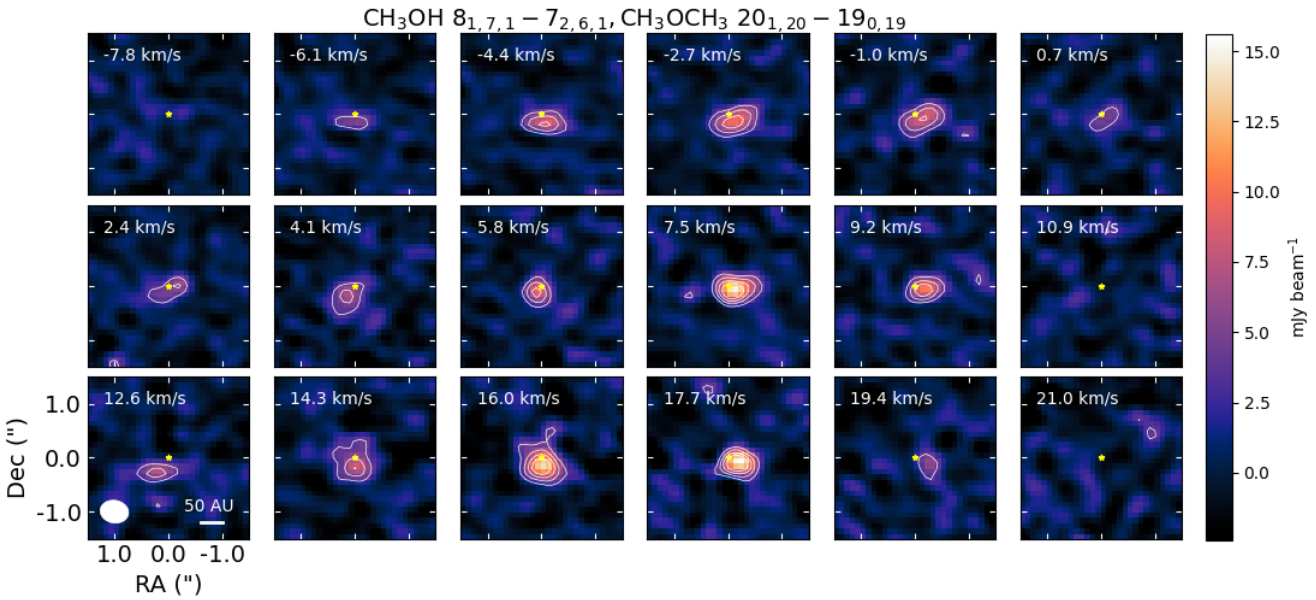

Fig. C.1. Channel maps of blended dimethyl ether and methanol lines. The first two rows show the two sets of dimethyl ether transitions while the bottom row shows emission coming from the methanol. The beam is shown in the bottom left corner and the scale bar is shown in the bottom right corner. Contours show the [3,5,7,9]×σ levels.

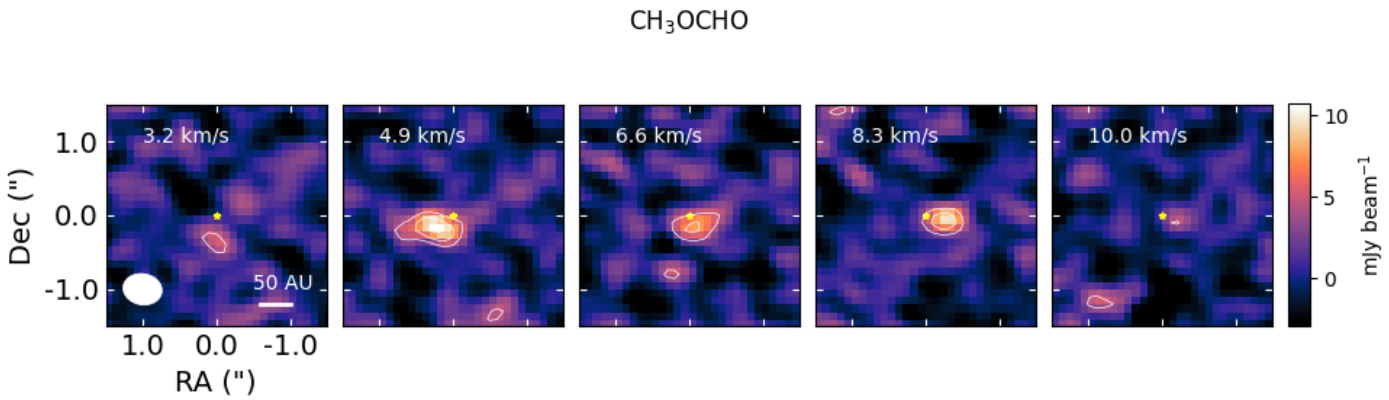

Fig. C.2. Channel maps of the methyl formate detection. The beam is shown in the bottom left corner and the scale bar is shown in the bottom right corner. Contours show the [3,5]×σ levels.